OPTICAL REVIEW Vol. 20, No. 5 (2013) 442–451

Numerical Evaluation of Linearized Image Reconstruction Based on Finite Element Method for Biomedical Photoacoustic Imaging

Shinpei Okawa*, Takeshi Hirasawa, Toshihiro Kushibiki, and Miya Ishihara

Department of Medical Engineering, National Defense Medical College, Tokorozawa, Saitama 359-8513, Japan

(Received February 19, 2013; revised May 10, 2013; Accepted July 2, 2013)

An image reconstruction algorithm for biomedical photoacoustic imaging is discussed. The algorithm solves the inverse problem of the photoacoustic phenomenon in biological media and images the distribution of large optical absorption coefficients, which can indicate diseased tissues such as cancers with angiogenesis and the tissues labeled by exogenous photon absorbers. The linearized forward problem, which relates the absorption coefficients to the detected photoacoustic signals, is formulated by using photon diffusion and photoacoustic wave equations. Both partial differential equations are solved by a finite element method. The inverse problem is solved by truncated singular value decomposition, which reduces the effects of the measurement noise and the errors between forward modeling and actual measurement systems. The spatial resolution and the robustness to various factors affecting the image reconstruction are evaluated by numerical experiments with 2D geometry.

Keywords: photoacoustic imaging, photon diffusion equation, wave equation, finite element method, truncated singular value decomposition, inverse problem

1. Introduction

Photoacoustic imaging enables us to diagnose the tissues deep inside the body quantitatively. The tissues that absorb the photons emitted by a laser convert the light energy to heat. Then, the acoustic pressure is generated by the thermal expansion of the tissues. The acoustic pressure, which is called photoacoustic (PA) pressure, can be detected as a signal by ultrasonic transducers and can be used to locate the tissues excited by the laser. The signal intensity depends on the optical absorption coefficients of the tissues, and the absorption coefficient reflects the conditions of the tissues.[1–4)]

Some imaging modalities using light are noninvasive and take advantage of the wavelength dependences of materials absorbing light. A spectroscopic technique allows us to quantify the constituents included in the biological tissues and provides us with unique information useful for diagnoses. It is well known that near-infrared (NIR) light penetrates deeply inside the biological medium. Thus, NIR light is often used for biomedical imaging.[5–7)] However, the light is highly weakened by scattering and absorption by the background tissues that are not targeted in the measurement. As a result, it is difficult to obtain an image with high spatial resolution.

On the other hand, the ultrasonic pressure is less affected by the background than light. By exploiting the nature of the ultrasonic wave, PA imaging can obtain an image a few centimeters below the surface of the biological medium and has a high spatial resolution from 10 μm to 1 mm. It has been studied that some exogenous photon absorbers such as gold nano particles increase the PA signal intensity and can improve the quality of the PA image.[8)]

In the image reconstruction, imaging targets, which are PA signal sources and have some characteristics different from the background, are located by processing PA signals. It is readily possible to determine the distance between the target and the detector by using the speed of sound and the time-of-arrival of the PA pressure. Some methods originally used in ultrasound imaging, i.e., the delay-and-sum (DS) and circular backprojection methods, are applied to PA imaging. Using the PA wave equation, Xu and coworkers derived analytical reconstruction methods such as the Fourier-domain algorithm and universal backprojection.[9–11)]

Indeed, the acoustic properties of the media affect the PA signals and the images in the practical measurement. Treeby et al. proposed the time-reversal reconstruction method for the absorbing acoustic media and reported that the image intensity and spatial resolution are improved by introducing the acoustic absorption to the reconstruction.[12)]

By considering the propagation of light in the medium, the optical properties of the PA signal sources can be quantitatively estimated. The amplitude of the PA signal depends on the light absorbed by the target. Therefore, the algorithm for reconstructing the optical properties of the target needs to consider the light propagation, especially when the scattering and absorption of the light by the background are not negligible. Laufer et al. presented quantitative imaging of photon absorbers using a nonlinear model-based inversion scheme that simulates the propagation of photons.[13)] Yuan et al. reconstructed the optical absorption coefficient and other optical and acoustic properties in the media by finite element method (FEM)-based reconstruction.[14,15)]

Currently, there exists no standard method for reconstructing the optical properties from the PA signals, although various methods have been proposed recently.[16)] This is because the reconstruction methods involve some technical

*E-mail address: okawa@ndmc.ac.jp

problems. The image reconstruction methods have been demonstrated with 2D models because of the high computational cost, which is one of the technical problems to be addressed for developing useful image reconstruction methods. Generally, an image reconstruction method, such as the model-based inversion scheme, needs prior information and assumptions that are not correct. Thus, a method robust to the incorrect prior information is preferable. The effects of incorrect prior information and other factors including measurement noise should be carefully investigated for the methods. In various points as just described, the quantitative reconstruction of the optical properties from the PA signals is still under discussion. Partly for this reason, some conventional image reconstruction methods transferred from ultrasound imaging, such as the DS method, are often used for PA imaging.

We developed and evaluated a quantitative image reconstruction method in this study. The method was used to reconstruct the absorption coefficient of the target in the media with the background having optical absorption and scattering by solving an inverse problem. The photon diffusion equation (PDE) and PA wave equation were utilized for the image reconstruction. Both equations were solved by FEM in this study. Using FEM is a way to model the complex geometry and to deal with inhomogeneous optical and acoustical properties of the biological media for image reconstruction. We used a linearized reconstruction method. By linearizing the relationship between the absorption coefficient and the PA signal, the algorithm becomes computationally less intensive than the nonlinear model-based scheme. Truncated singular value decomposition was used to reduce the effect of the noise on the reconstructed image.

A certain linearized reconstruction method is described in the literature.[16] However, we have not found any report on the development of a linearized reconstruction method with FEM described in this paper. Through various numerical simulations instead of practical experiments, we investigated how various factors, such as the random measurement noise, size, and position of the target, affect the reconstructed image. The effect of the inhomogeneity of the background was also investigated. In this investigation, we evaluated the effect of the incorrect prior information. The comprehensive studies reported in this paper, which might have been complicated by practical experiments, revealed the advantages and disadvantages of the developed reconstruction method quantitatively.

2. Image Reconstruction Algorithm

2.1 Propagation of light

The light emitted by a nano second pulse laser is propagated through biological tissues. The background tissues scatter and absorb the light. The fraction of the light that reached the target tissue is absorbed and causes the PA pressure. The propagation of the light in the biological media is rigorously described by the radiative transfer equation (RTE). Although the use of the RTE is the most accurate method to calculate the propagation of light, it is computationally costly. Therefore, we use the PDE of the approximation of the RTE,[17]

$$\{-\nabla \cdot D(\boldsymbol{r})\nabla + \mu_a(\boldsymbol{r})\}\Phi(\boldsymbol{r}) = q(\boldsymbol{r}), \tag{1}$$

where $D = 1/(3\mu_s')$ is the diffusion coefficient depending on the reduced scattering coefficient μ_s', μ_a, the absorption coefficient, Φ, the fluence rate, and q, the light source of the position $\boldsymbol{r}$.

The boundary condition, $-\boldsymbol{n} \cdot D\nabla\Phi = \Phi/(2A)$, is often used where $\boldsymbol{n}$ is the outer normal vector at the boundary and A is the parameter that depends on the refractive index. We used FEM to solve the PDE for Φ.[18]

The successive processes, which are absorption of light by tissues, conversion of light energy to heat, and generation of PA pressure, occur in a much shorter time range than the PA pressure propagation. The thermal confinement condition is satisfied when assuming the use of a nano second pulse laser, which is typically used in PA imaging for biological tissues.[2,3] Simulations in the following sections also met the condition. Thus, we ignore the time dependence of PDE to calculate the light energy absorbed by tissues.

2.2 Propagation of PA pressure

As the tissues absorb light, the energy is converted to heat, and the thermal expansion of the target generates PA pressure. The PA pressure propagates in the medium and is detected by ultrasonic transducers. The detected PA signal is used for the image reconstruction. The propagation of the PA pressure is described by the PA wave equation,[2,3]

$$\left\{-\nabla^2 + \frac{1}{v^2}\frac{\partial^2}{\partial t^2}\right\} p(\boldsymbol{r}, t) = \frac{\beta}{C_p}\frac{\partial}{\partial t} H(\boldsymbol{r}, t), \tag{2}$$

where t represents time, v, the speed of sound in the biological media, p, the acoustic pressure, β, the thermal expansion coefficient, and C_p, the specific heat. $\beta/C_p = \Gamma$ is called the Grüneissen parameter, which represents the efficiency of the generation of PA pressure. H is the light energy absorbed by tissues instantaneously after the laser illumination, which is formulated as

$$H = \mu_a \Phi \delta(t). \tag{3}$$

Φ is obtained by solving Eq. (1).

The Green's function of Eq. (2) is known. The Poisson formula is also well known. The k-space method[19,20] is efficient for obtaining the solution of Eq. (2). We employed FEM because of its extendability for future works.

2.3 Image reconstruction

We attempt to reconstruct the absorption coefficients of the targets embedded in the biological medium as a quantitative image. The target has a larger absorption coefficient than the background. The target we assume is a tumor with angiogenesis and/or that labeled by an exogenous photon absorber, for example.

The background consists of normal tissues. The light emitted by a nano second pulse laser is diffusively propagated by the background that scatters and absorbs the light. Therefore, PA pressure is generated not only by the

absorption of the target but also by that of the background. We assume that the light has the NIR wavelength usually used in the biomedical measurement.

Let us assume that the optical properties of the background are given as $\bar{\mu}_s'(\boldsymbol{r})$ and $\bar{\mu}_a(\boldsymbol{r})$ by an experiment prior to the image reconstruction. Then, the fluence rate in the background, $\bar{\Phi} = \Phi(\bar{\mu}_a)$, is obtained by solving Eq. (1). The source of the PA pressure of the background is $\bar{H} = \bar{\mu}_a\bar{\Phi}$.

When $\bar{\mu}_a$ is perturbed by the existence of the target, the absorption coefficients in the medium are written as $\mu_a = \bar{\mu}_a + \Delta\mu_a(\boldsymbol{r})$. Then, the source of PA pressure is approximated by the following linearized formula:

$$H(\mu_a) = \bar{H} + J\Delta\mu_a, \tag{4}$$

where J is the differential coefficient of H at $\bar{\mu}_a$.

We discretize the functions of $\boldsymbol{r}$, such as Φ and μ_a, into N pixels. Φ and μ_a are N vectors with the number of pixels, N. $N \times N$ matrix J has $J_{ii} = \Phi_i + \mu_{a_i} \cdot \partial\Phi_i/\partial\mu_{a_i}$ and $J_{ij} = \mu_{a_i} \cdot \partial\Phi_i/\partial\mu_{a_j}$ as $i \neq j$, where $i,j = 1,2,\ldots,N$. $\partial\Phi_i/\partial\mu_{a_j}$ is calculated by the perturbation method on the basis of Eq. (1).

According to Eq. (2), the set of measured PA signals, $\boldsymbol{m}$, is related to H linearly with the system matrix L,

$$\boldsymbol{m} = L\boldsymbol{H}, \tag{5}$$

where $\boldsymbol{m}$ is the MT vector and L is the $MT \times N$ matrix when the PA signals having T temporal samples are detected by M detectors simultaneously during the measurement. A column of L consists of a PA signal generated by a single source having a unit strength. Thus, L is calculated by solving the PA wave equation in Eq. (2). $\boldsymbol{H}$ is the N vector that discretizes the PA source distribution.

By substituting Eq. (4) into Eq. (5), we obtain

$$\Delta\boldsymbol{m} = LJ\Delta\mu_a, \tag{6}$$

where $\Delta\boldsymbol{m} = \boldsymbol{m} - L\bar{H}$ is the difference between the actual and simulated background signals.

In this study, the partial differential equations, Eqs. (1) and (2), were solved by FEM. Then, Eqs. (5) and (6) were constructed with the scaled-down matrices and vectors to reduce the calculation cost in the image reconstruction process, although the precision of Eq. (6) as the forward model decreased. We set the pixel containing multiple FEM nodes, and then the average of the PA signals generated by the sources at FEM nodes in a single pixel was adopted as the contribution (meaning a single column of the matrix L) of a single-pixel PA source. J_{ij} was also the average over the nodes in a single pixel. The sum of the fluence rates within the pixel was used as Φ_i. It is preferable to calculate $L\bar{H}$ as precisely as possible with small pixels or FEM elements to minimize the error between the actual and simulated signals.

Equation (6) is solved by the truncated singular value decomposition (TSVD) method.[21] Smaller singular values of (LJ), which amplify the effects of noise and errors in $\Delta\boldsymbol{m}$, are truncated, and then the generalized inversion matrix $(LJ)^-$ is obtained. The optimal number of truncated singular values is determined by the generalized cross validation (GCV) method. The solution is obtained as

$$\widehat{\Delta\mu_a} = (LJ)^-\Delta\boldsymbol{m}. \tag{7}$$

Finally, the distribution of $\hat{\mu}_a = \bar{\mu}_a + \widehat{\Delta\mu_a}$ is reconstructed as an image. The positions and μ_a of the targets can be estimated in the reconstructed image.

3. Methods of Numerical Simulations

3.1 Overall conditions

3.1.1 Simulation of the measurement data

Figure 1 shows the 2D geometries used in the numerical simulations. The square medium had a 50 mm side. We assumed that the light source was at $(x, y) = (0\,\text{mm}, 25\,\text{mm})$, and that 16 ultrasound transducers were placed from $x = -14$ to 16 mm on $y = 25$ mm with an equal spacing of 2 mm. One of the transducers was at a position identical to that of the light source. We assumed that the transducers were ideal and pointwise non directional.

The light source having a wavelength in the NIR range was assumed. The optical properties of $\bar{\mu}_s' = 1.0\,\text{mm}^{-1}$ and $\bar{\mu}_a = 0.001\,\text{mm}^{-1}$ were assumed for a uniform background. $\bar{\mu}_a$ was also used as the mean value of the inhomogeneous background μ_a. The target was placed in the medium. We changed the μ_a, position, size, and number of targets for simulation.

To simulate the measured data, FEM was employed with 10,201 nodes and 20,000 triangular elements. The FEM nodes were distributed uniformly with an equal spacing of 0.5 mm. The Grüneissen parameter was set as unity, and the speed of PA pressure in the medium of 1500 m/s was used for the FEM calculation. A differential approximation with a time step of $\Delta t = 0.1\,\mu\text{s}$ was used to calculate time-dependent terms in Eq. (2). Equation (2) discretized by FEM was solved with an implicit scheme. The measurement period was assumed as 50 μs. The PA pressure generated by the background $L\bar{H}$ was calculated using the same FEM mesh to simulate $\boldsymbol{m}$. Gaussian random noise was also added to the simulated $\boldsymbol{m}$.

3.1.2 Image reconstruction

The image reconstruction was carried out on pixel basis. The medium was discretized into 625 pixels. In each pixel having 2 mm on one side, 25 FEM nodes were contained. The centers of the pixels represented the pixel positions and were located at x and y of even numbers $-24, -22, \ldots, 24$. The values in $\widehat{\Delta\mu_a}$ were placed at the centers of the pixels to construct the image. The homogeneous backgrounds of $\bar{\mu}_s' = 1.0\,\text{mm}^{-1}$ and $\bar{\mu}_a = 0.001\,\text{mm}^{-1}$ were given.

Because the simulated $\boldsymbol{m}$ was generated with a finer model of FEM, the mismatch between the models for simulating $\boldsymbol{m}$ and for reconstructing images resulted in the error in the reconstructed image. Therefore, the simulations of the image reconstruction in this study can avoid "inverse crime problem".[22] The optimal number of truncated singular values for TSVD that reduces effect of noise was searched among the numbers of 0, 10, 20, ..., and 600 by the GCV method.

The simulations for the following six cases in Sect. 3.2 were carried out to evaluate the performance of the image

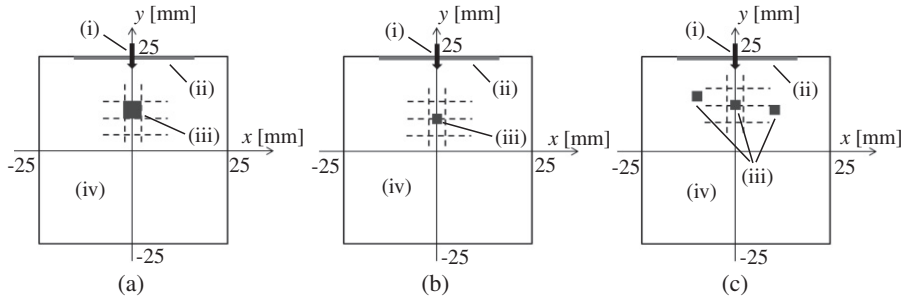

Fig. 1. 2D geometries in the numerical simulations with (i) light source, (ii) detector array, (iii) target(s) and (iv) background with constant or random μ_a for the cases where (a) the target fit with a single pixel for reconstruction, (b) the target did not fit within a single pixel, and (c) three targets did not fit within single pixels. Dashed lines illustrate the boundaries of the pixels.

reconstruction method. The full width at half maximum (FWHM) of the reconstructed target was measured after the spline interpolation of the $\hat{\mu}_a$ profile. All of the simulations and calculations were performed using Matlab (MathWorks).

3.2 Specific conditions

3.2.1 Effect of random measurement noise

Image reconstructions from $\boldsymbol{m}$ including Gaussian noise with various standard deviations were carried out. The geometry in Fig. 1(a) was used. The center of the true target with a 2 mm side was set at $(x, y) = (0\,\text{mm}, 16\,\text{mm})$. The true μ_a of the target was given as 0.002, 0.005, 0.010, or $0.020\,\text{mm}^{-1}$ to investigate the μ_a dependence of the reconstructed target. Gaussian noise was added to $\boldsymbol{m}$. The standard deviation of the Gaussian noise (SD_{noise}) was 0.01, 0.1, or 1.0% of the maximum value of $\boldsymbol{m}$. Five image reconstruction trials were conducted for every combination of the true μ_a of the target and SD_{noise}.

3.2.2 Dependence on size of true target

The reconstructions for the targets with various sizes were carried out. The geometry is depicted in Fig. 1(b). The true square target had a 1, 2, or 3 mm side. The size of the true target with a 1 mm side was smaller than the pixel, and the true target with a 3 mm side was larger than the pixel. The center of the true targets was at $(x, y) = (0\,\text{mm}, 15\,\text{mm})$, at which the boundary of two pixels crossed. That is, the true target laid within more than two pixels and did not fit with the positions and sizes of the single pixels. SD_{noise} was 0.01% of the maximum value of $\boldsymbol{m}$.

3.2.3 Dependence on depth of true target

The geometry in Fig. 1(a) was applied. The center of the true target having a 2 mm side was set at $y = 20$, 14, 8, or 2 mm on $x = 0$ mm so that the distance between the light source and the target was changed as 5, 11, 17, and 23 mm. This simulation was performed to investigate the depth dependence of the reconstructed target. Gaussian noise with an SD_{noise} of 0.01% was added to $\boldsymbol{m}$.

3.2.4 Effect of inhomogeneity of the background

The measured data $\boldsymbol{m}$ was simulated with the random and inhomogeneous distribution of the background μ_a to simulate the variations of the biological tissues. The true background μ_a was Gaussian-distributed with the standard deviation (SD_{bg}) of 10, 20, 30, or 40% of the mean value of $\bar{\mu}_a = 0.001\,\text{mm}^{-1}$. The geometry in Fig. 1(a) was used. The center of the true target with a 2 mm side was set at $(x, y) = (0\,\text{mm}, 14\,\text{mm})$. The μ_a of the true target was $0.01\,\text{mm}^{-1}$. Gaussian noise with an SD_{noise} of 0.01% was added to $\boldsymbol{m}$. For each SD_{bg}, the reconstruction was carried out with the forward model Eq. (6) by assuming a homogeneous background with $\bar{\mu}_a = 0.001\,\text{mm}^{-1}$. The effect of the mismatch between the background μ_a in the simulation of $\boldsymbol{m}$ and that in the assumption for the reconstruction process was investigated.

3.2.5 Comparison with a conventional method

The image reconstruction method developed in this study was compared with the DS method,[23] which was a conventional method. The DS method was a backprojection method. By summing the PA signals which are delayed depending on the distance between the detectors, and by projecting the sum of PA signals to the imaging region, the target can be located.

The geometry in Fig. 1(a) was used. The target fitting within a pixel had a 2 mm side. The true target was placed at $(x, y) = (0\,\text{mm}, 12\,\text{mm})$. The reconstructions were carried out for the following 2 cases: (i) a target with a unit source strength was in a transparent background with $\bar{\mu}_s' = 0\,\text{mm}^{-1}$ and $\bar{\mu}_a = 0\,\text{mm}^{-1}$. The proposed method solved the inverse problem formulated with Eq. (5) for $\boldsymbol{H}$, and (ii) the target with $\mu_a = 0.01\,\text{mm}^{-1}$ was in the scattering and absorbing uniform background. In both cases, the number and the positions of detectors were identical for both the developed and DS methods. The SD_{noise} was 0.01% of the maximum value of $\boldsymbol{m}$.

3.2.6 Image reconstruction affected by various factors

Finally, we attempted the image reconstruction from the simulated $\boldsymbol{m}$ contaminated by noise and the other factors we investigated in this study. The geometry in Fig. 1(c) was applied. Three true targets were assumed. Each target had a 1 mm side. This means that the sizes of the targets were smaller than the pixel. The centers of the targets were set at (i) $(x, y) = (-10\,\text{mm}, 15\,\text{mm})$, (ii) $(0\,\text{mm}, 13\,\text{mm})$, and (iii)

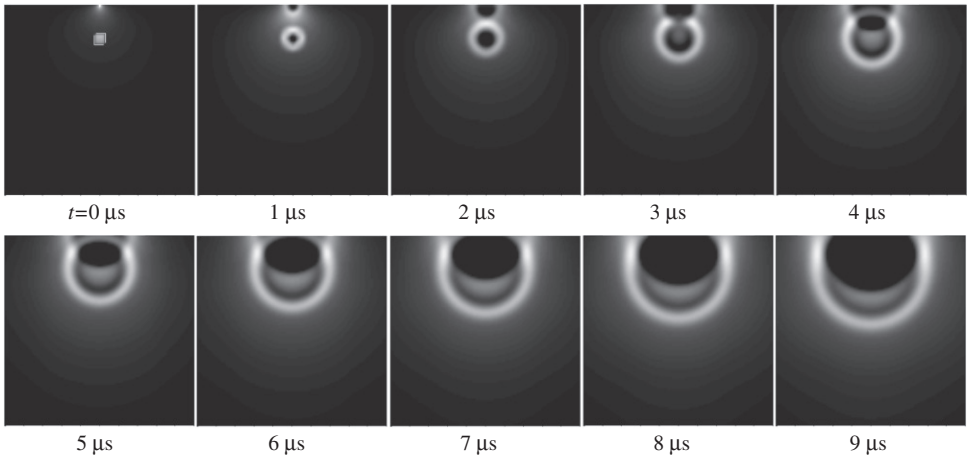

Fig. 2. Propagation of PA pressure in the case with the target with 2 mm side and $\mu_a = 0.01\,\mathrm{mm}^{-1}$ in the background medium with $\mu_a = 0.001\,\mathrm{mm}^{-1}$. The maximum PA pressure in each figure is displayed in white.

(10 mm, 11 mm). The distances from the positions (i), (ii), and (iii) were 14.1, 12.0, and 17.2 mm, respectively. The targets did not fit within single pixels. Every target had $\mu_a = 0.010\,\mathrm{mm}^{-1}$. The μ_a of the background was Gaussian-distributed with the mean value of $\bar{\mu}_a = 0.001\,\mathrm{mm}^{-1}$ and $SD_{bg} = 10\%$ of $\bar{\mu}_a$. Gaussian noise with $SD_{noise} = 0.1\%$ was added to the simulated $\boldsymbol{m}$. The image reconstructions were carried out with the assumption of the homogeneous distribution of $\bar{\mu}_a = 0.001\,\mathrm{mm}^{-1}$ in the background.

4. Results and Discussion

4.1 *Effect of random measurement noise*

Figure 2 shows the simulated propagation of PA pressure that generated $\boldsymbol{m}$ for the reconstruction. The target had $\mu_a = 0.01\,\mathrm{mm}^{-1}$. The initial PA pressure was generated instantaneously when the laser illuminated the medium at $t = 0\,\mu\mathrm{s}$. The PA pressure was generated not only by the target but also by the background. The maximum PA pressure existed at the illumination position and $t = 0\,\mu\mathrm{s}$. The PA pressure from the target was observed at the detector at $(x, y) = (0\,\mathrm{mm}, 25\,\mathrm{mm})$ about 6 μs after the illumination. The maximum PA pressure was about 23-fold of the PA pressure from the target detected at the illumination position. Note that the Gaussian noise added to $\boldsymbol{m}$ was determined by SD_{noise} and the maximum $\boldsymbol{m}$. Thus the noise with $SD_{noise} = 1\%$ was equal to that with the standard deviation of 23% of the signal from the target with $\mu_a = 0.01\,\mathrm{mm}^{-1}$. The result of the simulation of the PA pressure propagation was physically reasonable. A finer FEM meshing could indeed provide a more precise result.

The reconstructed images of the true μ_a of the target of $0.01\,\mathrm{mm}^{-1}$ are shown in Fig. 3. The maximum $\hat{\mu}_a$ was observed at the true position of the target for each SD_{noise}. Because the time-of-arrival of PA pressure directly indicates the distance between the PA source and the detector, the position of the target was robustly estimated by PA imaging.

On the other hand, the size of the reconstructed target increased with increasing SD_{noise}. It is also apparent that the maximum $\hat{\mu}_a$ decreased. We observed that the larger the

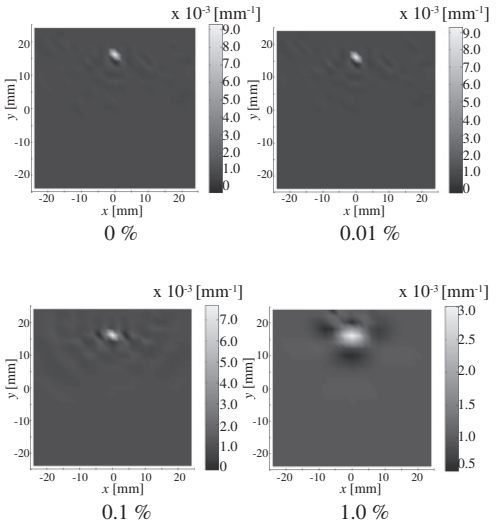

Fig. 3. Reconstructed images of μ_a from PA signals with random measurement noise with $SD_{noise} = 0$, 0.01, 0.1, and 1.0%. The true μ_a of the target was $0.01\,\mathrm{mm}^{-1}$.

SD_{noise}, the larger the number of truncated singular values. The TSVD method reduced the effect of the noise, and the target was reconstructed clearly even when $SD_{noise} = 1\%$. However, the truncation eliminated small differences between the contributions of neighboring PA sources to $\boldsymbol{m}$. Therefore, it became difficult to recover the precise distribution of μ_a, and as a result, the image was blurred, as shown in Fig. 3. It was not possible to reconstruct the target without TSVD in this simulation.

Figure 4(a) shows the maximum $\widehat{\Delta\mu_a}$ as a function of true $\Delta\mu_a$. The $\widehat{\Delta\mu_a}$ of the target decreased as SD_{noise} increased. When SD_{noise} was less than 1%, $\widehat{\Delta\mu_a}$ had a good linear relationship with the true value. Because of the mismatch between the FEM meshing for the generation of $\boldsymbol{m}$ and the pixels for the reconstruction, $\hat{\mu}_a$ did not agree completely with the true values, even when $SD_{noise} = 0\%$. Owing to the linearized approximation in Eq. (4), the difference between

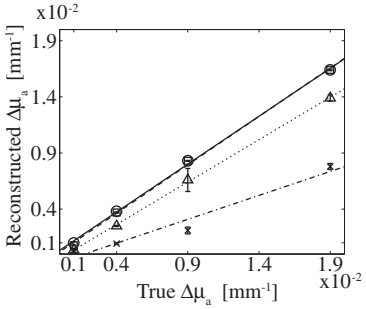

(a)

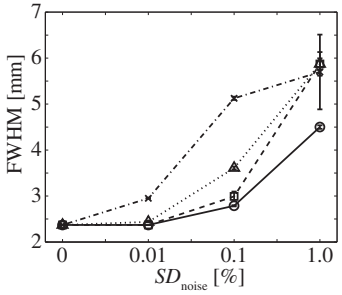

(b)

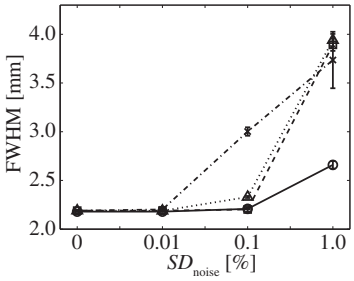

(c)

Fig. 4. (a) Reconstructed $\Delta\mu_a$ of the target as a function of the true $\Delta\mu_a$ with the regression lines for SD_{noise} of 0 (circles and solid line), 0.01 (squares and dashed line), 0.1 (triangles and dotted line), and 1.0% (x's and chained line). (b) FWHM of the reconstructed target along x-axis and (c) FWHM of the reconstructed target along y-axis for true $\Delta\mu_a$ of the target of 0.019 (circles and solid line), 0.009 (squares and dashed line), 0.004 (triangles and dotted line), and 0.001 mm^{-1} (x's and chained line).

$\widehat{\Delta\mu_a}$ and true $\Delta\mu_a$ increased with increasing true $\Delta\mu_a$. The linearized method successfully recovered $\Delta\mu_a$ values up to 0.009 mm^{-1} when SD_{noise} was less than 1% in this simulation.

FWHMs of the reconstructed target along the x- and y-axes are shown in Figs. 4(b) and 4(c), respectively. When the true $\Delta\mu_a$ was small, the FWHM increased significantly. This is because the signal-to-noise ratio (SNR) of the target with small $\Delta\mu_a$ was relatively small. The effect of TSVD mentioned above is seen in Figs. 4(b) and 4(c) again.

4.2 *Dependence on size of true target*

The reconstructed images with the various sizes of the true targets are shown in Fig. 5, and Fig. 6 shows $\widehat{\Delta\mu_a}$ and FWHM. The image with the true target of 1 mm is similar to that of 2 mm. It is impossible to distinguish the targets

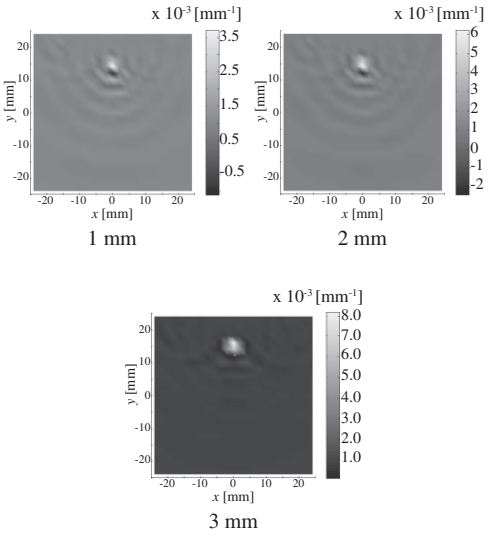

Fig. 5. Reconstructed images of μ_a in cases with the sizes of the true targets having 1, 2, and 3 mm sides.

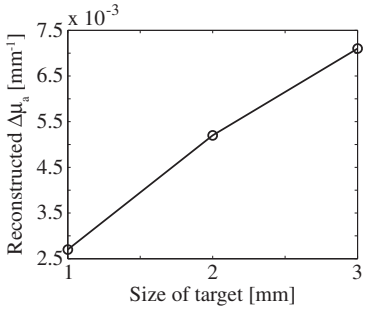

(a)

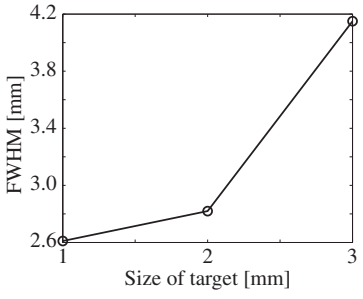

(b)

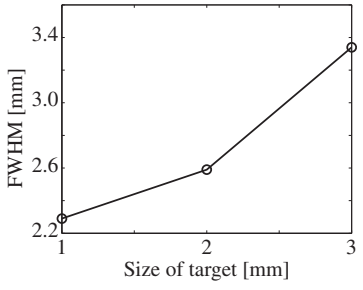

(c)

Fig. 6. (a) Reconstructed $\Delta\mu_a$ of the target, (b) FWHM of the reconstructed target along x-axis, and (c) FWHM of the reconstructed target along y-axis as functions of the size of the true target.

smaller than the pixel from the pixel-sized target. The difference between the two images can be seen in the values of $\hat{\mu}_a$. $\widehat{\Delta\mu_a}$ with the 2 mm true target was almost twice as large as that with the 1 mm true target. The the reconstruction method attributed the difference in PA signal intensity to the difference in μ_a, although the difference in PA signal intensity was actually caused by the difference in true size.

On the other hand, the reconstructed target with a true size of 3 mm was larger than that with a true size of 2 mm. The FWHM with the 3 mm true target was about 1.4 times as large as that with the 2 mm one. The target larger than the pixel can be reconstructed depending on the size. The light absorption increased with increasing target size. Therefore, the $\widehat{\Delta\mu_a}$ of the target with a true size of 3 mm became larger than that of the target with a true size of 2 mm as plotted in Fig. 6, although it was not identical to the true value. The linearized method reconstructs the images reflecting the true size of the target in some ways.

Note that the size of the 2 mm true target was the same as the pixel but did not fit within a single pixel. In this case, the FWHM in Fig. 6 became slightly larger than that under a similar condition ($SD_{noise} = 0.01\%$ and true $\Delta\mu_a = 0.009\,mm^{-1}$) in the previous simulation shown in Fig. 4. The target lying astride multiple pixels was reconstructed in this simulation. The $\widehat{\Delta\mu_a}$ of the target in this simulation was about 60% of that in the previous simulation. This result indicates that the small positional mismatch between the true target and the pixel for reconstruction affects the reconstructed target. The simulations in this section suggest that the pixel size should be appropriately determined by considering the spatial resolution and precision of $\widehat{\Delta\mu_a}$ required for the application of the PA image reconstruction method.

4.3 *Dependence on depth of true target*

It is shown in Fig. 7 that the reconstructed target depended on the depth at which the true target existed. The $\widehat{\Delta\mu_a}$ of the target decreased, as shown in Fig. 8(a). The deeper the position of the true target, the wider the area of the target. The FWHM along the *x*-axis steeply increased, as shown in Fig. 8(b), although the FWHM along the *y*-axis in Fig. 8(c) hardly changed. The FWHMs along the *x*-axis at the depths of 17 and 23 mm were twofold and threefold that at 5 mm, respectively. This result can be explained by the following two reasons (i) and (ii).

(i) The wide target located parallel to the detector surface in Fig. 7 can generate $\boldsymbol{m}$ similarly to the simulated $\boldsymbol{m}$ used in this simulation. As the true pointwise target is embedded deeply in the medium, the distance of the propagation, which is the radius of the circular wavefront, from the detector surface is long. Then, the PA pressure, which becomes similar to a plane wave, reaches multiple neighboring detectors at one time. The wide target can also generate the PA pressure arrives at the multiple detectors at one time. It is difficult for the reconstruction algorithm to distinguish the source distributions generating similar measured data, and the TSVD method tends to reconstruct a smooth and wide PA source rather than a pointwise one.

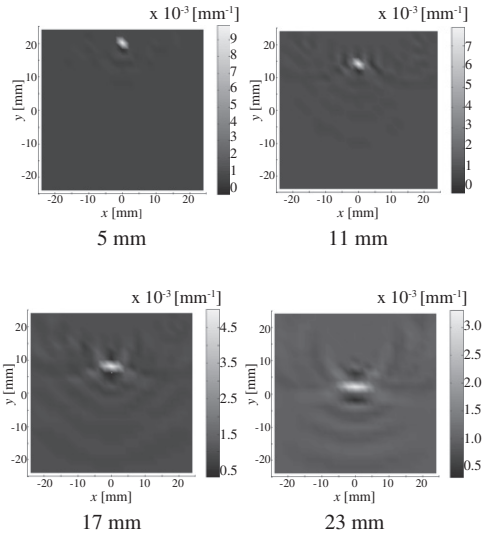

Fig. 7. Reconstructed images of μ_a in cases with the distances between the light source and the targets of 5, 11, 17, and 23 mm.

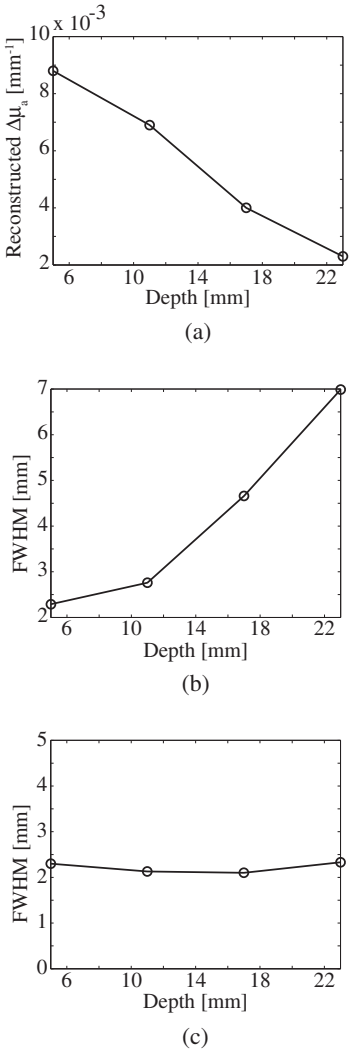

Fig. 8. (a) Reconstructed $\Delta\mu_a$ of the target, (b) FWHM of the reconstructed target along *x*-axis, and (c) FWHM of the reconstructed target along *y*-axis as functions of the distance between the light source and the true target.

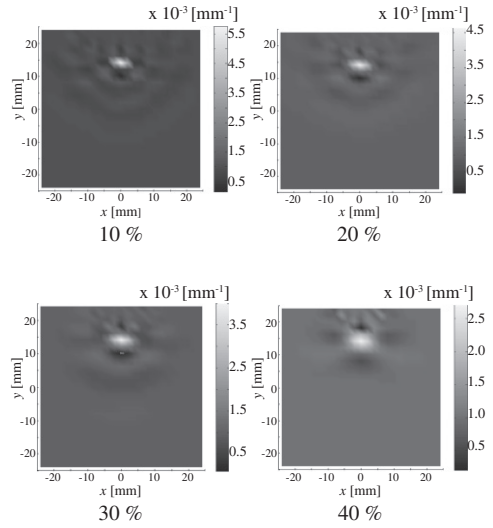

Fig. 9. Reconstructed images of μ_a in cases with the inhomogeneous backgrounds with $SD_{bg} = 10$, 20, 30, and 40%.

(ii) Additive noise made it difficult to identify a localized target. The strength of the source placed far from the light source is low, because Φ is small owing to the decay of the light. Additionally, the PA pressure is attenuated during the propagation. The SNR was not sufficiently large to localize the pointwise target.

4.4 *Effect of inhomogeneity of the background*

The background μ_a, which was randomly distributed, affected the spatial resolution of the reconstructed image. The reconstructed target was blurred, as shown in Fig. 9. Figure 10(a) shows the $\widehat{\Delta\mu_a}$ of the target, which decreased with increasing SD_{bg}. The FWHM with $SD_{bg} = 40\%$ was twofold that with 10%, as shown in Figs. 10(b) and 10(c). Although the quality of the reconstructed image was lowered by the effect of the mismatches between the actual and assumed μ_a values, the target was reconstructed at a the correct position robustly. It is impossible to reduce the variation in the μ_a of tissues in vivo, but it can be said that prior information about the optical properties of the background medium is a key to a successful image reconstruction.

If some tissues or organs that are not targeted in the imaging but strongly absorb the light unexpectedly exist in the medium, those can be reconstructed and may affect the reconstruction of the target. It is difficult to distinguish the target and nontargeted tissues only by the image reconstruction method in this study. Some prior information about the structure of the medium obtained by other imaging modalities, such as ultrasound imaging and magnetic resonance imaging, provide a method for interpreting the reconstructed PA image accurately. Multispectral measurement must also be useful.

4.5 *Comparison with a conventional method*

Figure 11 shows the reconstructed images in cases (i) and (ii). Note that the DS method reconstructed the image of the region narrower than that considered in the developed method, because the DS method basically projected the PA signals along the vertical lines on which the detectors were located. As the DS method projects the intensities of PA signals to the imaging region, the DS method does not reconstruct μ_a quantitatively. The DS method located the position of the PA signal source.

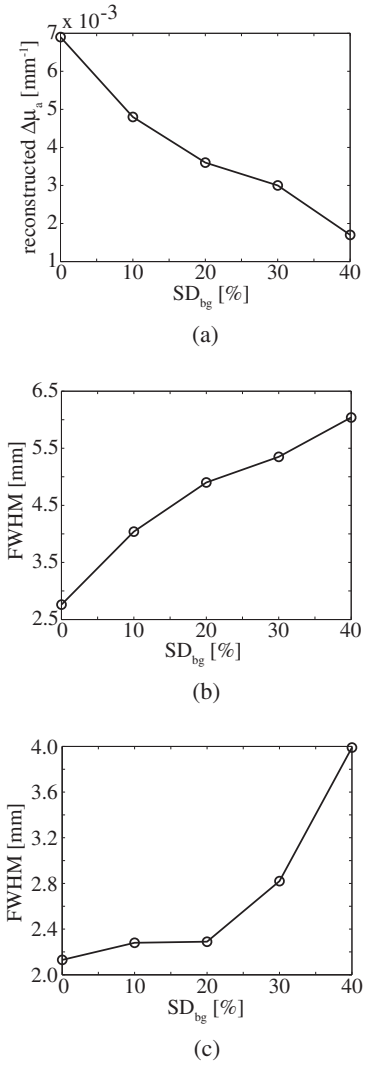

Fig. 10. (a) Reconstructed $\Delta\mu_a$ of the target, (b) FWHM of the reconstructed target along x-axis, and (c) FWHM of the reconstructed target along y-axis as functions of SD_{bg}.

In case (i), the target was correctly located by both methods. The FWHMs on the x- and y-axes of the target reconstructed by the DS method were 6.3 and 3.6 mm, while those of the target reconstructed by the developed method were 2.5 and 2.2 mm, respectively. The developed method reconstructed the target clearly localized at the correct position. The FWHM with the developed method was about half of that with the DS method. The reconstructed source strength of the target was 93% of the true unit strength. The reconstructed $\boldsymbol{H}$ in a transparent medium can be readily transformed into μ_a by using Eq. (3) and the Beer-Lambert law.

On the other hand, the target can be barely seen in the image reconstructed by the DS method for case (ii). Owing to the absorption of the background, the maximum of the PA source was reconstructed at the illumination position. Indeed, a small peak of the PA source, which was 8% of the maximum, was reconstructed at the correct position. The FWHMs of the target reconstructed by the DS method along the x- and y-axes were 5.8 and 2.8 mm, respectively. When the PA signal is noisy or the background is inhomogeneous, it may be impossible for DS method to locate the target. The developed method reconstructed the target at the correct position clearly as well as in case (i). The FWHMs with the developed method along the x- and y-axes were 3.2 and 2.1 mm, respectively. The reconstructed μ_a of 0.0069 mm^{-1} was slightly smaller than the true value owing to the effect of the depth of the true target.

The developed method reconstructed the image with a wider area than that considered in the DS method, although the area depends on the directivity and sensitivity of the detectors. Additionally, the spatial resolution of the developed method was superior to that of the DS method in this simulation with a relatively small number of detectors. By taking the light propagation in the scattering and absorbing background into account, the developed method localized the target clearly and reconstructed μ_a quantitatively. The differences between the developed method and other conventional methods, such as circular backprojection and the Fourier transform method, seem to be similar to those pointed out in this section, according to the literature.[23)]

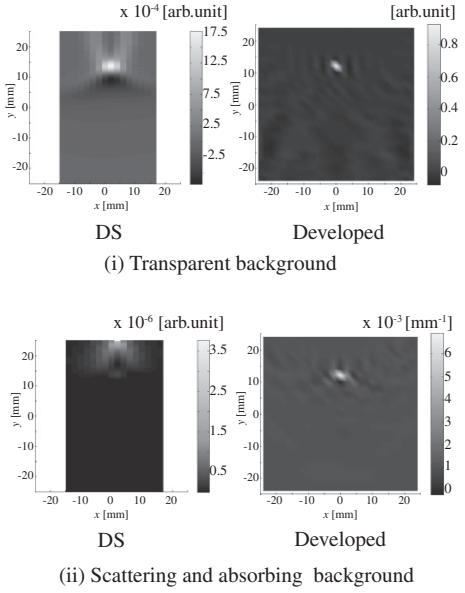

Fig. 11. Images reconstructed by DS and developed methods for (i) the transparent background and (ii) the scattering and absorbing background.

4.6 *Image reconstruction affected by various factors*

The results of the simulation to generate the PA signals are shown in Fig. 12. In addition, the PA pressures were generated by three targets, and a strong PA pressure propagated from the illumination position. Figure 13 shows the reconstructed image. Three $\hat{\mu}_a$ peaks were reconstructed at $(x, y) = (-10\,\text{mm}, 16\,\text{mm})$, $(0\,\text{mm}, 14\,\text{mm})$, and $(10\,\text{mm}, 10\,\text{mm})$, which are the pixels closest to the true potions of the targets (i), (ii), and (iii), respectively. The targets were reconstructed in the correct pixels. Various noises and mismatches considered in this simulation caused low spatial resolutions. The reconstructed targets were larger than the true ones. The reconstructed FWHMs along the x-axis were 5.8, 5.3, and 6.6 mm for the targets (i)–(iii), respectively. The FWHMs along the y-axis were 3.4, 2.8, and 4.2 mm for the target (i)–(iii), respectively. Noise and mismatch also caused underestimation of μ_a. The peak values of $\hat{\mu}_a$ were 1.7×10^{-3}, 2.0×10^{-3}, and 1.5×10^{-3} mm^{-1} for the targets (i)–(iii), respectively.

The target in the position (ii) was reconstructed better than the other targets because the distance from the light source to the position (ii) was smaller than those from the light source

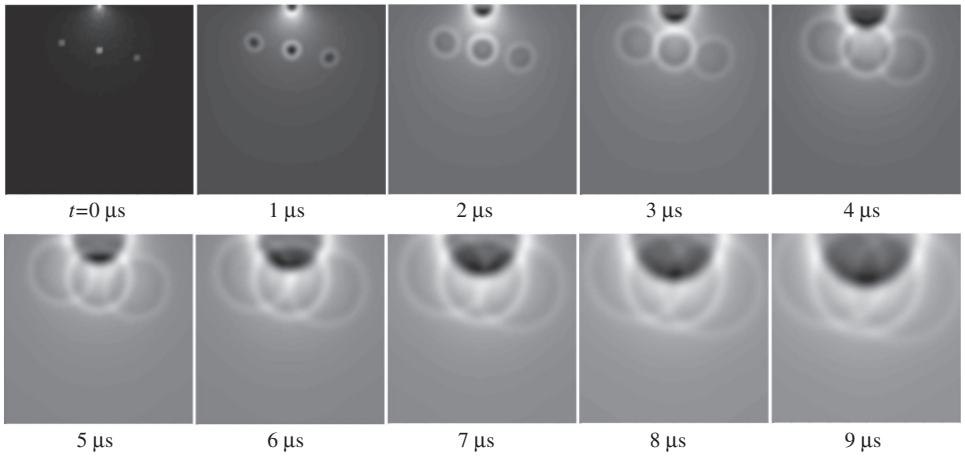

Fig. 12. Propagation of PA pressure in case with three targets with a 1 mm side having $\mu_a = 0.01\,\text{mm}^{-1}$ in the inhomogeneous background medium with $\mu_a = 0.001\,\text{mm}^{-1}$ and $SD_{bg} = 10\%$. The maximum PA pressure in each figure is shown in white.

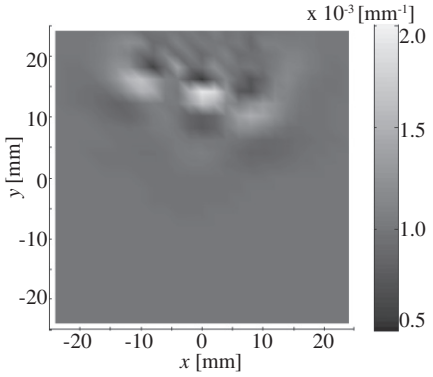

Fig. 13. Reconstructed image of μ_a in the case with various factors.

to the positions (i) and (iii). The closer the target to the light source, the better the reconstruction of the target. This result is consistent with the results of the previous simulations. The PA signal originated from the target near the light source had a higher SNR; thus, the FWHM of the reconstructed target was smaller and $\widehat{\Delta\mu_a}$ was larger. To reconstruct the target deeply embedded in the medium, it is important increasing the SNR as much as possible.

5. Conclusions

The linearized image reconstruction was numerically evaluated in this paper. The forward model was constructed by FEM. The relationship between the absorption coefficient and the PA signal intensity was linearized using the PDE and PA wave equation. The linearized inverse problem in reconstructing the absorption coefficient of the target in the medium was formulated. The linearized inverse problem was solved by the TSVD method in this study.

It was demonstrated that various factors including the random measurement noise, positions of the targets and mismatches in forward modeling affect the reconstructed images. Precise forward modeling will provide high-quality images, and the high SNR of PA signals improves the spatial resolution and the estimation of the absorption coefficient especially when the target is deeply embedded in the medium. Additionally, the TSVD method robustly reconstructed the targets in various cases with noisy data and mismatches in forward modeling in this study. It is helpful to use a certain regularization technique to solve the inverse problem for robust image reconstruction.

Acknowledgements

This work was partially supported by JST Collaborative Research Based on Industrial Demand (In vivo Molecular Imaging: Towards Biophotonics Innovations in Medicine) and JSPS KAKENHI (Grant Number 24760314).

References

1) L. V. Wang and S. Hu: Science **335** (2012) 1458.
2) M. Xu and L. V. Wang: Rev. Sci. Instrum. **77** (2006) 041101.
3) C. Li and L. V. Wang: Phys. Med. Biol. **54** (2009) R59.
4) S. Hu and L. V. Wang: J. Biomed. Opt. **15** (2010) 011101.
5) A. P. Gibson, J. C. Hebden, and S. R. Arridge: Phys. Med. Biol. **50** (2005) R1.
6) T. Yates, J. C. Hebden, A. Gibson, N. Everdell, S. R. Arridge, and M. Douek: Phys. Med. Biol. **50** (2005) 2503.
7) R. Fukuzawa, S. Okawa, S. Matsuhashi, T. Kusaka, Y. Tanikawa, Y. Hoshi, F. Gao, and Y. Yamada: J. Biomed. Opt. **16** (2011) 116022.
8) Y.-S. Chen, W. Frey, S. Kim, P. Kruizinga, K. Homan, and S. Emelianov: Nano Lett. **11** (2011) 348.
9) M. Xu, Y. Xu, and L. V. Wang: IEEE Trans. Biomed. Eng. **50** (2003) 1086.
10) M. Xu and L. V. Wang: Phys. Rev. E **71** (2005) 016706.
11) Y. Xu, D. Feng, and L. V. Wang: IEEE Trans. Med. Imaging **21** (2002) 823.
12) B. E. Treeby, E. Z. Zhang, and B. T. Cox: Inverse Probl. **26** (2010) 115003.
13) J. Laufer, B. Cox, E. Zhang, and P. Beard: Appl. Opt. **49** (2010) 1219.
14) H. Jiang, Z. Yuan, and X. Gu: J. Opt. Soc. Am. A **23** (2006) 878.
15) Z. Yuan, Q. Wang, and H. Jiang: Opt. Express **15** (2007) 18076.
16) B. Cox, J. G. Laufer, S. R. Arridge, and P. C. Beard: J. Biomed. Opt. **17** (2012) 061202.
17) S. R. Arridge: Inverse Probl. **15** (1999) R41.
18) M. Schweiger, S. R. Arridge, and D. T. Delpy: J. Math. Imaging Vision **3** (1993) 263.
19) B. T. Cox and P. C. Beard: J. Acoust. Soc. Am. **117** (2005) 3616.
20) B. T. Cox, S. Kara, S. R. Arridge, and P. C. Beard: J. Acoust. Soc. Am. **121** (2007) 3453.
21) C. R. Vogel: *Computational Methods for Inverse Problems* (SIAM, Philadelphia, PA, 2002).
22) S. Holder: *Electrical Impedance Tomography: Methods, History and Applications* (IOP Publishing, Bristol, U.K., 2005).
23) J. I. Sperl, K. Zell, P. Menzenbach, C. Haisch, S. Ketzer, M. Marquart, H. Koenig, and M. W. Vogel: Proc. SPIE **6631** (2007) 663103.